GALILEO NET FLUX RADIOMETER EXPERIMENT

L. A. SROMOVSKY, F. A. BEST, H. E. REVERCOMB

Space Science and Engineering Center, University of Wisconsin-Madison, WI 53706, U.S.A.

and

J. HAYDEN

Martin Marietta Astronautics Group, U.S.A.

Abstract. The Galileo Net Flux Radiometer (NFR) is a Probe instrument designed to measure the vertical profile of upward and net radiation fluxes in five spectral bands spanning the range from solar to far infrared wavelengths. These unique measurements within Jupiter's atmosphere, from which radiative heating and cooling profiles will be derived, will contribute to our understanding of Jovian atmospheric dynamics, to the detection of cloud layers and determination of their opacities, and to the estimation of water vapor abundance. The NFR uses an array of pyroelectric detectors and individual bandpass filters in a sealed detector package. The detector package and optics rotate as a unit to provide chopping between views of upward and downward radiation fluxes. This arrangement makes possible the measurement of small net fluxes in the presence of large ambient fluxes. A microprocessor-controlled electronics package handles instrument operation.

1. Introduction

The Galileo Probe Net Flux Radiometer (NFR) is designed to measure the net radiation flux and upward radiation flux within Jupiter's atmosphere as the Probe descends by parachute. The nominal measurement regime for the NFR extends from about 0.1 bar to at least 10 bars, which corresponds to an altitude range from 48 km above the 1-bar level to 91 km below it. These measurements will help to define sources and sinks of planetary radiation, regions of solar energy deposition, and provide constraints on atmospheric composition (primarily water vapor). The instrument was designed and built by Martin Marietta, later modified to incorporate design improvements developed at the University of Wisconsin-Madison where the instrument was calibrated. The NFR Principal Investigator is L.A. Sromovsky of the University of Wisconsin-Madison, and the Co-Investigators are J. Pollack of Ames Research Center, M. Tomasko of the University of Arizona, J. Hayden of Martin Marietta Astronautics Group, and H. Revercomb, also from the University of Wisconsin.

Following a brief description of the scientific objectives of the experiment, we describe the instrument hardware, how it functions, and how it is calibrated. Finally, we present a brief summary of expected errors and performance characteristics.

2. Scientific Objectives

2.1. Measuring driving forces for atmospheric circulation

Absorbed solar radiation and the flux of energy from the planet's interior provide the primary drive for atmospheric motions in Jupiter's atmosphere. Because solar radiation

Space Science Reviews **60:** 233–262, 1992.

absorption and planetary emission occur at different places and altitudes, net atmospheric heating and cooling result in buoyancy differences which force atmospheric motions. An understanding of Jovian circulation thus requires knowledge of the vertical profile of radiative heating and cooling and its horizontal distribution as well.

The NFR measurements contribute to this understanding by measuring the net radiation flux as a function of altitude. This net flux, the difference between upward and downward radiation powers crossing a horizontal surface per unit area, is directly related to the radiative heating or cooling of the local atmosphere: the radiative power per unit area absorbed by an atmospheric layer is equal to the difference in net fluxes at the boundaries of the layer. At any point in the atmosphere radiative power absorbed per unit volume is thus given by the vertical derivative of net flux (dF/dz), and the corresponding heating rate is just $dT/dt = (dF/dz)/(\rho C_p)$, where ρ is the local atmospheric density and C_p is the local atmospheric specific heat at constant pressure.

2.2. Objectives of Spectral Flux Measurements

Because the Galileo Probe will provide only one sample profile of Jovian atmospheric conditions at one location, it is especially important to understand why the measured radiative energy deposition occurs: we might then have some idea of how to apply the results to other atmospheric regions which were not sampled. The NFR experiment contributes to understanding horizontal variations by making spectral measurements which illuminate the mechanisms by which radiation interacts with the atmosphere. When these are interpreted with other Probe measurements and linked with Orbiter observations they provide a basis for using orbiter observations to extend radiative heating determinations to other locations on the planet (Hunten *et al.*, 1986).

Using six detector channels, the NFR measures net and upward flux densities in five spectral bands. The specific objectives of each channel are briefly described in the following paragraphs and also summarized in Table I.

TABLE I

Summary of NFR spectral channels and objectives

Channel	Bandpass	Objective
A	3–500 μm	Deposition/loss of thermal radiation
B	0.3–3.5 μm	Total deposition of solar radiation
C	3.5–5.8 μm	Water vapor and cloud structure
D	14–35 μm	Water vapor
E	0.6–3.5 μm	Solar deposition in methane absorption region
F	Blind	Witness to detector perturbations

Channel *A*: *Spectral range from 3 to 500 μm* (the broadband thermal channel). Net flux measurements define sources and sinks of planetary radiation. When used with calculations of gas opacity effects, these observations define the thermal opacity of particulates, which is much harder to calculate.

Channel *B*: *Spectral range from 0.3 to 3.5 μm* (the broadband solar channel). Net flux

measurements determine the solar energy deposition profile; upflux measurements help discriminate between cloud particle absorption and extinction.

Channel *C*: *Spectral range from 3.5 to 5.8 μm* (the excess thermal channel). Net flux and upward flux measurements define the excess thermal energy emitted by Jupiter within this atmospheric window; this channel is very sensitive to both cloud opacity and the water vapor mixing ratio and will be used also to constrain other measurements of water.

Channel *D*: *Spectral range from 14 to 35 μm* (the water vapor channel). Net flux measurements define regions of combined hydrogen and water vapor absorption; water vapor will be deduced from deviations from known hydrogen effects. Where atmospheric opacity is high, net flux in this channel will be proportional to the product of local opacity (unknown) and the local temperature gradient (independently measured).

Channel *E*: *Spectral range from 0.6 to 3.5 μm* (the methane channel). Net flux and upward flux measurements in this band are strongly affected by cloud particles as are the broader band channel *B* measurements, but channel *E* is proportionately more strongly affected by methane band absorption; comparison with the broader band measurements of channel *B* will allow a 'methane-free' determination of cloud particle absorption effects.

Channel *F*: *A spectrally blind channel* (the witness channel). Measurements by this detector provide information needed to correct for extraneous detector perturbations.

It should be noted that none of the NFR measurements is really a direct measurement which is unencumbered by the need to assume some characteristics of the parameters to be measured. Rather than measuring net flux directly, the NFR samples the angular domain and weights non-uniformly the spectral variations in the radiation field. To interpret these measurements requires modelling of the radiation field as a function of composition, cloud, and thermal structure. The measurements then provide strong constraints on the models rather than provide direct determinations of model parameters.

3. Instrument Description

3.1. Physical configuration

The NFR consists of two major sub-assemblies: the electronics module (EM), and optical head (OH), shown mated together in Figure 1. The electronics module is about 13 cm × 19.5 cm × 16 cm high while the optical head is about 8.5 cm × 8 cm high × 10.5 cm long. The total weight of the NFR is 3.134 kg, of which 0.672 kg is due to the optical head. The electronics module has four feet which are bolted to the Probe instrument shelf. The optical head, supported only by its attachment to the electronics module, extends out of the Probe through the Probe thermal blanket and aeroshell to allow the NFR sensors to view atmospheric radiation.

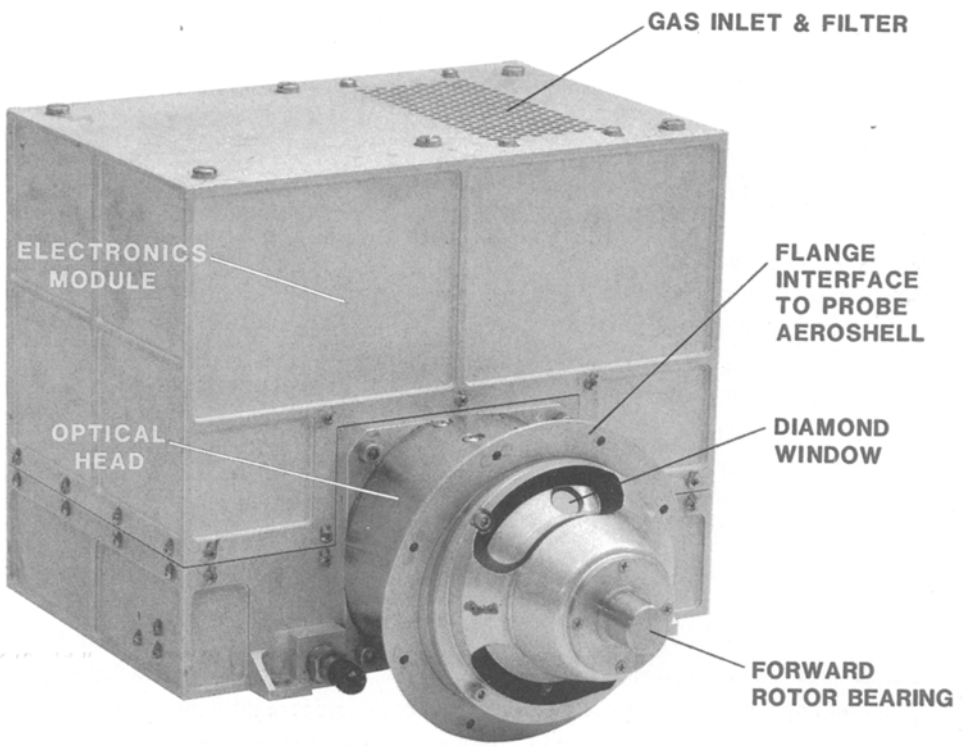

Fig. 1. Physical configuration of the NFR instrument. The total length of the optical head is approximately 10.5 cm. The part of the optical head beyond the flange is directly exposed to the ambient Jovian environment.

Optical Head

The NFR optical head, shown in cutaway view in Figure 2, contains optics, detectors, and preamplifiers which rotate as a unit as they chop between upward and downward atmospheric views, or between ambient and internal heated black-bodies for on-board calibration measurements. Flexible circuits carry power to the preamplifiers and analog signals from the pre-amplifiers to the electronics module for further processing. The rotating optics assembly is supported by a front and rear bearing and driven through a gear by a stepper motor. The front housing, which supports the front bearing, has two apertures through which atmospheric radiation can reach the diamond window. A curved band, or shroud, is attached to the rotating optics to restrict the flow of gas through the front housing apertures no matter what position the window is in.

Optics and Field of View

The optical system, shown in Figure 3, consist of a diamond window, a folding mirror, a toroidal mirror, a condensing cone, and spectral filters which are part of the detector package. An unfolded diagram of the optics is shown in Figure 3(b). The toroidal mirror images the diamond window at the entrance to the condensing cone. The detector and

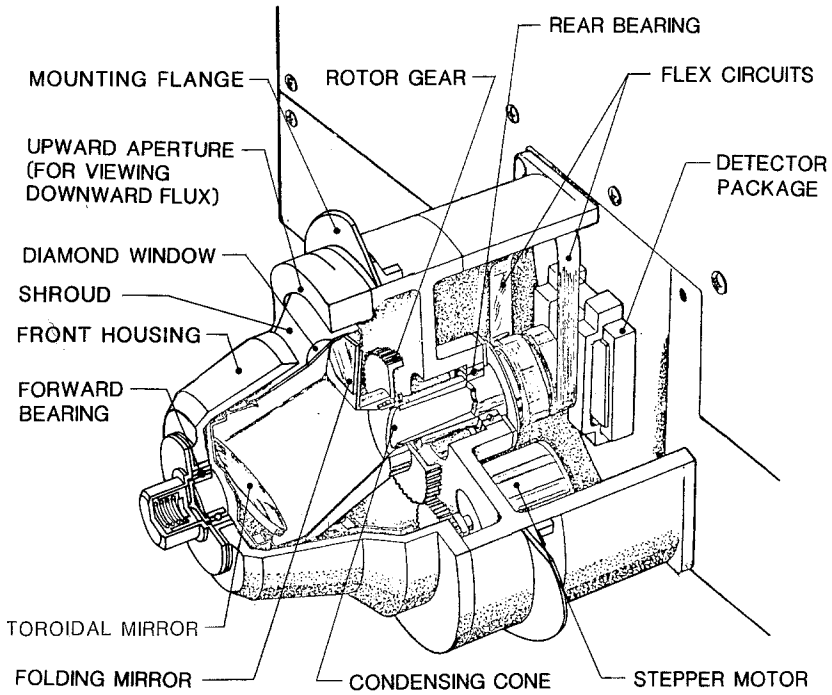

Fig. 2. NFR Optical Head. During net flux measurements the detector package and optics rotate between upward and downward viewing positions, which are respectively 45° below and above horizontal. Though it is not shown in this diagram, the front housing also has a bottom aperture to allow viewing upward flux (see Figure 1).

three mirror images are imaged approximately 0.76″ behind the diamond window. This arrangement allows the detector to be positioned in a thermally isolated location while still achieving a relatively large field of view of nominally 0.4 sr ($\pm$ 20° about the nominal viewing directions of 45° above and below horizontal).

Because of viewing and thermal constraints on the instrument, the NFR samples only part of upward and downward radiation fields, rather than integrating over the entire hemispheres. Thus, the NFR actually measures a weighted net spectral radiance rather than a net flux. The viewing directions of $\pm$ 45° from horizontal, instead of $\pm$ 90°, actually provide a more representative sample because the largest contribution to the net flux occurs at $\pm$ 45° (when solid-angle weighting is included).

Detector Package

All NFR spectral channels use pyroelectric thermal detectors to convert absorbed radiation power to electrical signals (the operation of these detectors is described in a following section on analog signal characteristics). The NFR detector package contains an array of six lithium tantalate detectors mounted in close proximity on a single circuit board (Figure 4). This circuit board is bonded to a hermetically sealed hybrid pre-amplifier package to which the detectors are electrically connected (Figure 5). Spectral

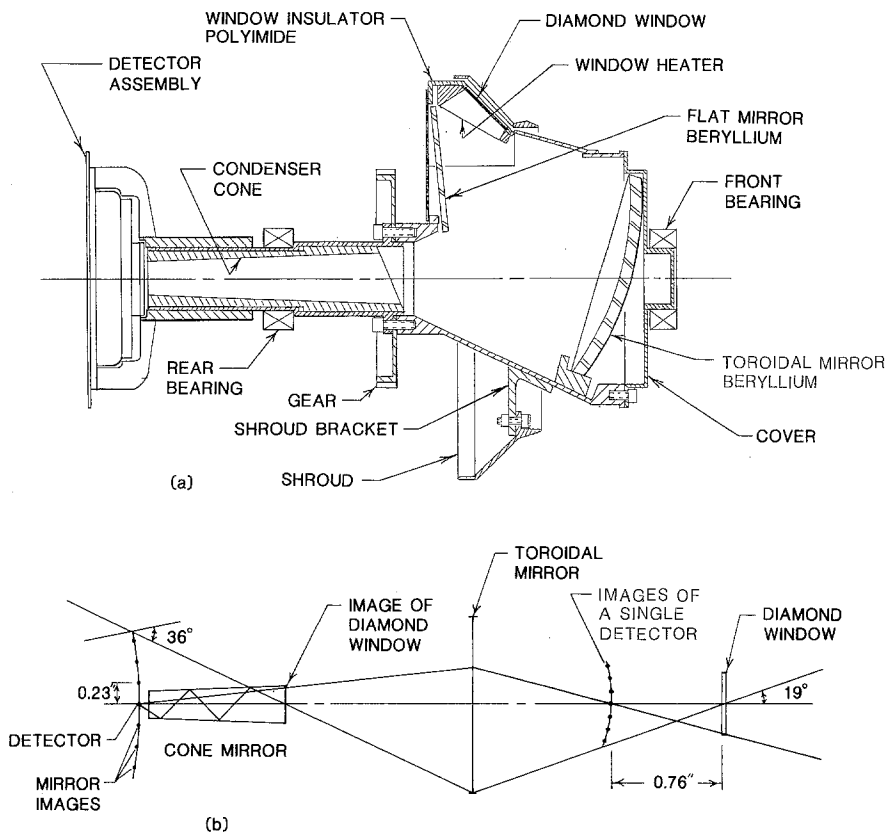

Fig. 3. Rotating optics layout (a) and unfolded ray-trace diagram (b). The condenser cone reflects three annular images of the detectors which the toroidal mirror brings to a focus 0.76″ behind the diamond window together with the prime image. The diameter of the base of the condenser cone is just large enough to prevent obscuration of the six-detector array. The diamond window is focussed at the entrance to the condenser cone.

filters are mounted in a filter frame which is pin-located and screw-mounted to the detector circuit board. The location pins (see Figure 4) are also used in detector fabrication to insure proper positioning of the detector elements relative to the filter frame openings.

The detectors were fabricated by Infrared Associates of Cranbury, New Jersey. Each pyroelectric detector element consists of a $LiTaO_3$ crystal approximately 1 mm × 2 mm × 25 μ (about 0.001″ thick). Lithium tantalate was chosen as the pyroelectric material because it has a Curie point well above the expected operating temperature and thus would not become depolarized. The NFR detector elements have unusually smooth edges because they are cut from a larger piece of crystal using ion-beam milling instead of a diamond saw. These smooth edges result in crystals which are exceptionally rugged. The bottom electrode of each element is opaque gold and is applied before the detector material is cut into individual elements. The top electrode

Fig. 4. Detector module photograph. The six pyroelectric elements in the center of the photograph have been overexposed to make them more visible (the paint coating the detectors is much blacker than it appears in this photo). Detector leads are soldered to eyelets which are connected to runs on the back side of the detector circuit board. The alignment pins are used during fabrication as well as for positioning the filter frame. Each detector element is approximately 1 mm × 2 mm.

is vacuum-deposited after the elements are mounted in the array and consists of a transparent layer of nichrome with small gold pads deposited for lead bonding. Platinum leads of 12.5 μ diameter are attached to top and bottom electrodes using electrically conductive epoxy. (The other ends of the leads are soldered to the circuit board.) The top electrode is sized to match the desired active area and is somewhat smaller than the crystal itself. Black paint (3M velvet) is applied to the top surface so as to cover the active area but not the entire detector. The typical paint thickness is 20–25 μ (slightly less than 0.001″). Because $LiTaO_3$ is a piezoelectric material, as well as a pyroelectric, the detector elements are mounted on 0.015″-high mesas made of a vibration dampening material called Visilox.

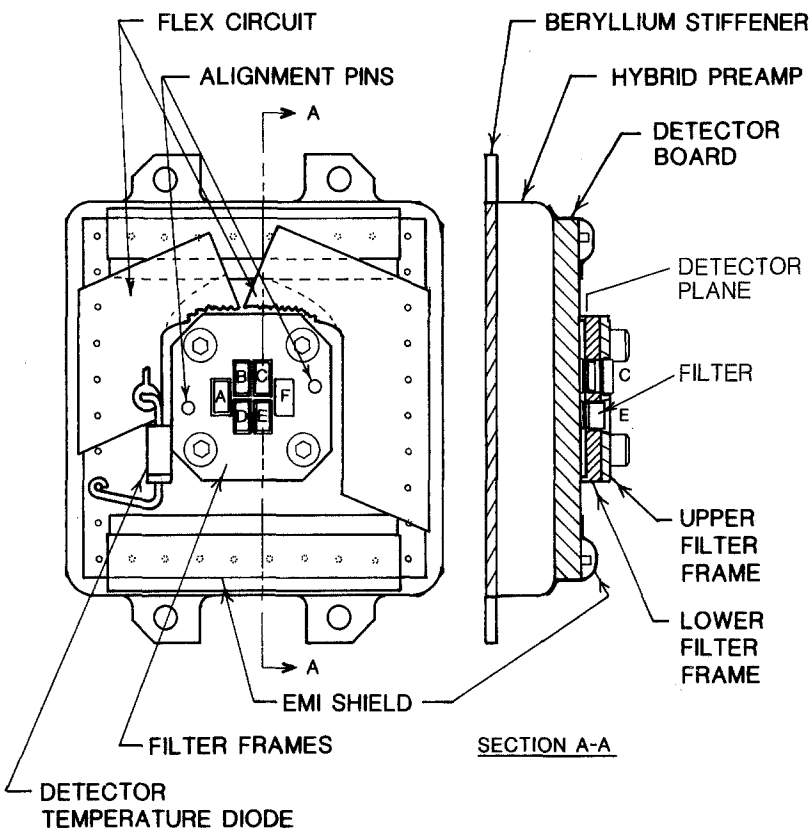

Fig. 5. NFR Detector/Hybrid Assembly. This drawing shows a 1″ × 1″ detector module bonded to the preamplifier can, which is in turn bonded to a beryllium stiffener. Upper and lower filter frames are shown mounted above the detector array. Note that a stack of two filter elements is used for channel *C*. The 0.033 cm^3 volume enclosed between the filter frame and the detectors (shown in the side view) is sealed and back-filled with xenon.

Detectors have a primary thermal time constant of approximately 110 ms, an electrical capacitance of about 40 pF, and a responsivity of approximately 1400 V/W. Noise associated with the detectors is generally dominated by Johnson noise of the detector load resistor.

The spectral filter materials and thicknesses are listed in Table II. (All channels experience additional spectral filtering by the 0.2 mm thick diamond window at the entrance to the rotating optics, the spectral reflectivity of the mirrors, and the spectral response of the detectors.) As indicated in Figure 5, there are two filter frames: an upper frame containing only a CaF_2 long-wave blocker for channel *C*, and a lower filter frame containing five spectral filters and one opaque blocker for the blind channel. All filters are epoxy bonded in place on shelves machined into the filter frame.

The detector package is hermetically sealed and backfilled with xenon gas at ambient pressure (about 800 mb). The seal alone eliminates an extreme sensitivity to external

TABLE II

NFR Spectral Filters. In the following table MLC denotes multi-layer interference coating. Filter thicknesses are approximate.

Channel	Bandpass	Upper filter	Lower filter
A	3–500 μm	none	MLC on 0.1 mm diamond
B	0.3–3.5 μm	none	Corning 056, 1.5 mm
C	3.5–5.8 μm	1 mm CaF_2	MLC on 1 mm Si
D	14–35 μm	none	MLC on 0.5 mm Ge
E	0.6–3.5 μm	none	Corning 2–64
F	Blind	none	Blocker

pressure modulations. The backfill of the very heavy xenon gas is used to buffer the small amount of hydrogen gas which will diffuse into the detector package during descent. The buffering effect maintains a low thermal conductivity inside the detector package and thereby eliminates significant thermal crosstalk which otherwise would occur via gas conduction between detector elements. Other benefits of the seal include making the detector responsivity independent of external pressure and protecting detector interior coatings and lead bonds from ambient atmospheric conditions. The seal is accomplished first by sealing the filters into the lower filter frame (then leak testing and patching if required). The second step is to epoxy both the lower and upper filter frame on the detector board with a hypodermic needle temporarily replacing one of the alignment pins. The needle provides access to the sealed volume so that leak testing and patching can be carried out until all leaks are sealed. The detector package (with hypodermic) is then backfilled with xenon and placed in a glove box filled with xenon. Within the glove box the hypodermic needle is removed and an alignment pin is epoxied in its place to complete the seal. After the epoxy is cured the entire package is leak tested using a radiometric technique to verify absence of a gross leak and then with a mass spectrometer scanning over the xenon peak to measure the fine leak. A leak rate of approximately 7×10^{-10} cc s^{-1} or less (of Xe at STP) was measured for the flight detector package, implying that about 100 mb of Xe will be present inside the detector package at entry, ensuring that the seal objectives will be met (see later discussion of expected performance).

Internal Sources

When the optical system is not viewing external radiation, it views one of two internal radiation sources: an ambient black-body source which is thermally coupled to the wall of the front housing, and a heated black-body source which is servo-controlled to a temperature of approximately 107 °C (the servo point is attained in air or vacuum, but generally is not attained in He or H_2 atmospheres where high gas conductivity limits the black-body temperature to a maximum differential above the ambient atmospheric temperature). By chopping the view between these two internal sources it is possible to carry out approximate internal calibrations during laboratory testing and as part of

in-flight checkouts during the cruise phase of the mission. However, during the descent into the Jovian atmosphere, the hot black-body will operate much closer to the temperature of the ambient black-body and the accuracy of internal calibrations will not be very high.

Motor

A 90° step^{-1}, bipolar, 2-phase stepper motor and a 2 to 1 gear set are used to rotate the optics and detector system. Each step of the motor results in 45° of motion for the optics. Following the convention defined in Figure 6, the upward viewing position of the

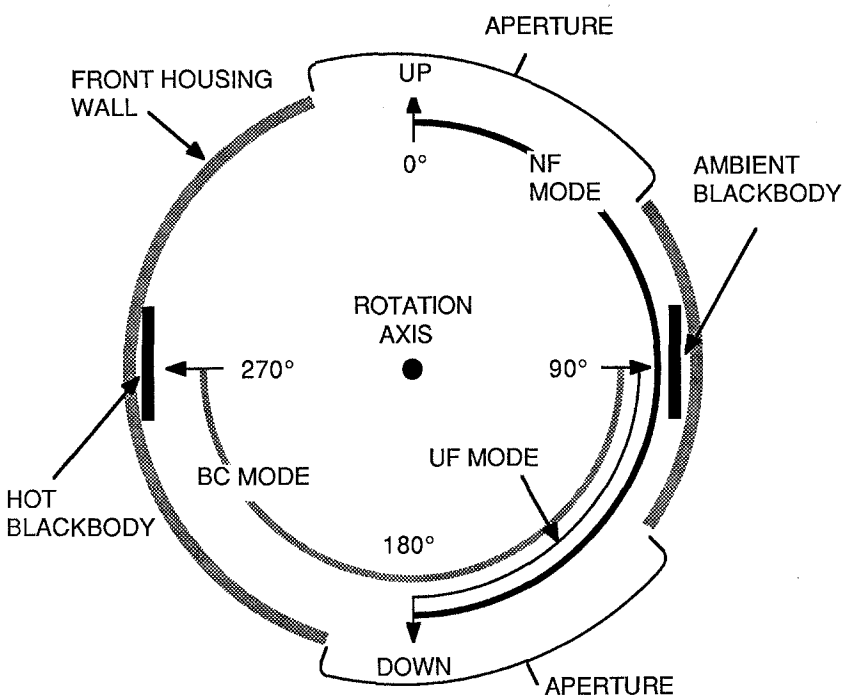

Fig. 6. NFR operating modes diagram, viewed from the rear of the optical head looking towards the nose. Cyclical NFR rotor motion is indicated by arcs for Net Flux (NF), Up Flux (UF), and Black-body Calibrate (BC) modes of operation. A hard stop prevents viewing near 315°. Radial arrows indicate viewing directions at the ends of each arc.

optics is defined to be at 0°, the ambient black-body position at 90°, the downward view at 180°, and the hot black-body at 270°. The motor has torque sufficient to move the rotor 180° in about 60 ms.

Window Heater

A 300 mW heater is used to maintain the external diamond window slightly warmer than the ambient atmosphere, thereby preventing condensation on the window.

Optical Head Ventilation Design

Because the rotating optics could not structurally support a high-pressure differential, the interior of the rotating optics is not sealed, and will admit ambient external gas during descent. Thermal modelling of the NFR shows that the detector package temperature will lag behind the external atmospheric temperature during all but the early part of descent. To inhibit possible condensation on interior optical surfaces, gas flow into the rotor is controlled by vents within the electronics module and at the base of the rotor. These vents take advantage of the dynamic pressure distribution around the Galileo descent Probe which provides a positive pressure differential between the inside of the Probe and the external atmosphere in the vicinity of the NFR apertures. The predicted gas flow is first into the Probe through a large vent at the back of the Probe. Some of this gas enters the electronics module through a Line 5A molecular sieve filter provided at the top of the electronics (see Figure 1). The filtered gas, also warmed by the electronics module, enters the rear of the optical head through a vent provided at the base of the electronics module. From this point the gas flows partly into the rotor through the rotor base vent (near the rear bearing) and partly through the motor and rotor bearings into the forward part of the optical head and then through the apertures into the external atmosphere. The differential pressure driving this flow is approximately 1 mb and at 1 atm the total flow rate through the optical head will be approximately 100 cc s^{-1}.

Method of Operation

The various modes of NFR operation are illustrated in Figure 6. To perform the net flux measurement the motor first positions the optics at 0°, then alternately cycles 4 steps down (45°, 90°, 135°, and 180°) and 4 steps up (135°, 90°, 45°, 0°). The optics is cycled down and up twice each second. During approximately 60 ms of each half cycle the optics is in transition, leaving approximately 190 ms for staring up or down. Eleven up-down cycles of the optics are integrated to make one net flux instrument cycle (IC) which is transmitted to the Probe data system at a rate of one IC every 6 s. Up flux and blackbody calibrate instrument cycles are performed in a similar fashion. To make an up flux measurement the rotor is first positioned at 90° to view the ambient blackbody then alternately cycled between down (180°) and the ambient blackbody (90°). For blackbody calibration, the optics is first positioned to view the ambient blackbody (90°) then cycled between the hot black-body (170°) and the ambient blackbody.

During the last powered pulse of each half of a chopping cycle the unpowered of the two motor coils is electrically shorted to activate eddy-current damping which provides greater stability of motion and more accurate pointing (especially in the Up Flux mode). A set of position sensors is used to verify correct rotor positioning within 5° of the nominal position. The LEDs used to stimulate the position sensors may degrade substantially during radiation exposure and therefore cannot be relied on to verify pointing during descent. However, LED degradation will not affect motor operation since the motor is driven with an open loop system which does not require position feedback.

Mode Sequences

The NFR operating modes are carried out in a sequence which repeats at 2-min intervals. Each complete sequence, called a data cycle (DC), consists of 20 six-second ICs. As defined in Table III, each DC uses one IC for the Blackbody Calibrate (BC) sample, one for the Up Flux (UF) sample, and one for Analog Zero (AZ), to be explained later. This leaves 17 ICs available for Net Flux (NF) measurements. Because of offset level shifts between different input sources, the net flux measurements following AZ and UF modes are 'short-cycled', meaning that only the last five of the eleven up-down flip cycles are included in the measurement. All AZ measurements, except the first, are also short-cycled because they immediately follow the large offset developed during the BC mode. Housekeeping data, listed at the right side of Table III, provides information on temperatures, voltages, and currents (the acronyms used here are defined in the table caption).

3.2. Electronics

A functional block diagram of the NFR electronics is shown in Figure 7. The design is centered around a CMOS microprocessor control system very similar to that used

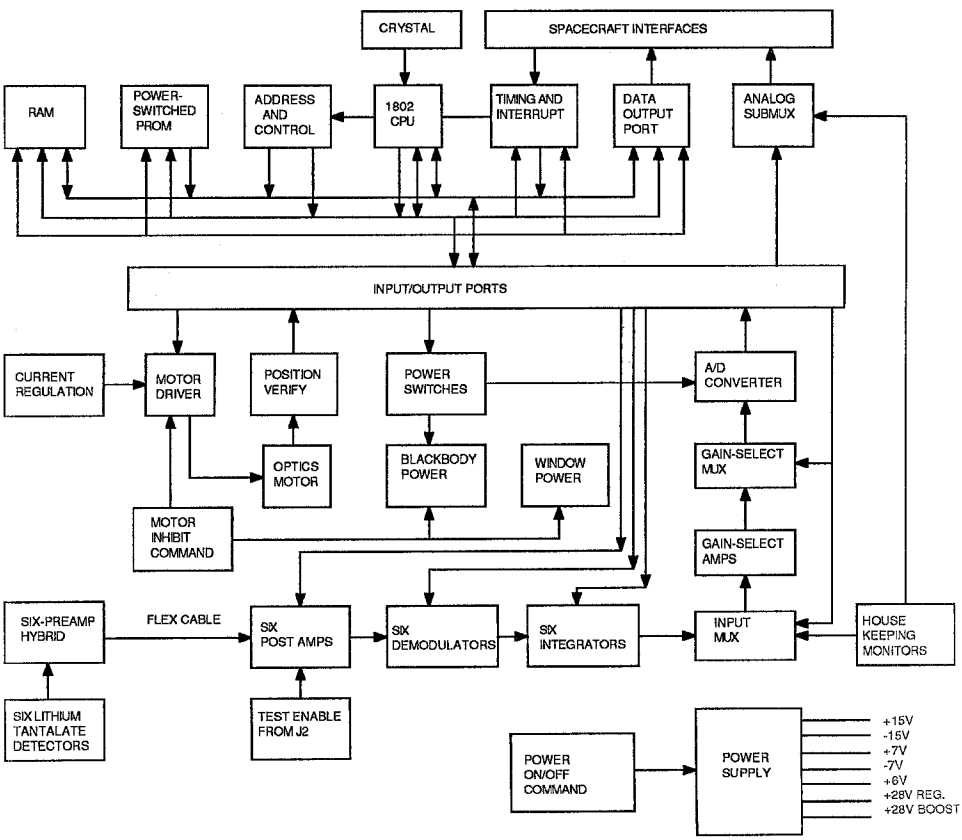

Fig. 7. Electronics block diagram. Instrument operation is controlled by software stored in PROMs.

TABLE III

NFR Data Cycle (DC) contents. Each row defines the data output for each instrument cycle (IC). AZ denotes analog zero, NF denotes net flux, UF denotes up flux, and BC denotes blackbody calibration. HB and BI denote the temperature and approximate current of the internal hot blackbody. A1 and A2 denote low range and high range thermistor measurements of the ambient blackbody. WT and WI denote window temperature and window heater current respectively. Detector temperature is denoted by DET and electronics temperature by ET. V1 and V2 denote voltage data for + 10 V ADC reference and + 7 V supply respectively. GSAC1, 8, 64 denote calibration data for gain-select amplifers, while GSAZ1, 8, 64 denote zero data for the gain select amplifiers.

IC	Time (s)	Mode	Flips used	Housekeeping
0	6	AZ	5	HB, A1
1	12	NF	5	A2, WT, WI
2	18	NF	11	V2, A2
3	24	NF	11	GSAC1, DET, A1, A2
4	30	NF	11	ET, WT, BI
5	36	NF	11	SW, SW
6	42	NF	11	GSAZ1, V1, WT
7	48	NF	11	DET, A1, A2
8	54	NF	11	HB, WT
9	60	UF	5	GSAC8, HB, WT, BI
10	66	NF	5	HB, WT
11	72	NF	11	DET, A1, A2
12	78	NF	11	V2, A1, WI
13	84	NF	11	GSAZ8, A2, WT
14	90	NF	11	ET, WT
15	96	NF	11	DET, A1, A2, BI
16	102	NF	11	GSAC64, V1, WT
17	108	NF	11	A1, A2, WI
18	114	NF	11	HB, WT
19	120	BC	11	GSAZ64, DET, HB, A2

on the Atmospheric Structure Instrument (ASI) for the Galileo Probe (Seiff *et al.*, 1990). Functional elements of the NFR electronics are described in the following paragraphs.

Digital Circuits

The microprocessor system consists of the 1802 CPU (Central Processing Unit), 256 words of RAM (Random Access Memory), 6144 8-bit words of PROM (Programmable Read-Only Memory), nine I/O (Input/Output) ports and a power-up reset circuit. The RAM is used to provide 256 bytes of temporary storage for data values during data accumulation and manipulation. The six 1-Kbyte PROMs contain the program necessary to operate the instrument. At any given time only the one of the six PROMS is turned on and for only 1 μs of the 8 μs machine cycle, providing a factor of 48 reduction of power consumption by the PROMs. Six 8-bit wide output ports are used to control the non-digital NFR subsystems. Three input ports are used to read data from the NFR subsystems.

The 2048 Hz spacecraft clock is divided down to a 4-Hz signal which is used to interrupt the microprocessor. The MINOR FRAME signal from the spacecraft is used

to synchronize the 4-Hz timer and also to synchronize the software with spacecraft timing. The software does not begin cycling in its normal mode until the microprocessor detects a MINOR FRAME interrupt.

The PROM software controls the sequence, timing, and duration of motor control pulses. After each cycle of the optical rotor, position sensor photo transistors are read to determine if the optics are at the correct position. If any one of the 22 half cycles of one instrument cycle (IC) results in an incorrect optics position, the microprocessor notes this in the data stream by setting the motor position error bit to one for that IC.

Analog Circuits

There are six channels of analog processors, one for each detector. Each channel includes a detector signal pre-amplifier, a post-amplifier, a demodulator and an integrator. This six pre-amplifiers are housed in a hybrid package placed adjacent to the detectors on the rotating optics (see Figure 5). The rest of the analog circuits reside on two circuit boards within the electronics module.

Pre-Amplifiers

Each pre-amplifier is a DC differential amplifier with a gain of 6.67, using U423 dual JFET inputs. The effective input load resistance of $0.909 \times 10^{10}\ \Omega$ ($10^{10}\ \Omega$ in parallel with $10^{11}\ \Omega$) in combination with the typical detector capacitance of 40 pF leads to a detector electrical droop time constant of 0.36 s. With this droop a typical detector will generate an electrical offset of 0.055 V per $^{\circ}$C min^{-1} of thermal ramp. During descent we expect a thermal ramp less than 7 $^{\circ}$C min^{-1}, so that the input offset will not exceed 0.38 V, comfortably less than the pre-amplifier saturation level of about 0.75 V. Because the load resistance so much less than the $10^{13}\ \Omega$ detector resistance, detector noise is dominated by the Johnson noise of the load resistors (modified by the detector shunt capacitance, of course).

Post-Amplifiers

The six parallel post-amplifiers each consists of three non-inverting amplifiers in series (except for channels *B* and *E* which have one inversion to correct for an inversion built into the detector package). Single pole RC filters are used to block the DC component from the hybrid and to tailor the frequency response of the circuit. The filter components are chosen to give a maximum response at 16 Hz. This may seem strange in view of our fundamental 2 Hz detector signal. However, this filter function acts somewhat like a differentiator, which, in combination with the following integrator, results in a very small sensitivity to the details of signal transitions and a high sensitivity only to the final values attained after each flip of the rotor. This effect minimizes asymmetry errors (described in a subsequent section).

FET (Field Effect Transistor) switches at the input of each post amplifier allow the inputs to be grounded through a 100 Ω resistor, providing a zero reading to be integrated as the Analog Zero (AZ) data. The AZ value is intended to be a measure of offset in

the integration circuitry, but is also slightly affected by other factors which are still under investigation.

The gain of the post amplifiers is tailored to the dynamic range expected from each channel. To extend the dynamic range of channels *A*, *C*, and *D*, which receive much stronger signals from the internal heated black-body than they do from Jupiter's atmosphere, the third amplifiers of the circuits for those channels (and also for channel *F*) have two possible gains selectable with a FET switch. The gain is switched to 8 for analog zero (AZ), up flux (UF), and net flux (NF) measurements, and switched to unity for the black-body calibrate (BC) measurement. The solar channels, *B* and *E*, receive relatively weak signals from the on-board calibration source and thus do not need gain reduction capabilities.

Demodulator and Integrator

Each demodulator is a gain unity, reversible polarity amplifier, the polarity of which is controlled by two FET switches, synchronized to the 2-Hz NFR decommutation signal.

The integrator consists of an inverting amplifier with a 0.82 μF capacitor in the feedback loop and a 1 MΩ resistor connected between the output of the demodulator and the input to the integrating amplifier. A FET switch is placed in paralel with the capacitor to short out the charge after a measurement has been taken. Two other switches control input to the integrator. In one configuration the output of the demodulator is connected to the integrator (enabling integration); in the other configuration the demodulator output is disconnected and the integrator input is grounded (holding the integrated value for readout by the A/D converter).

Gain Select Amplifier (GSA)

All six integrator outputs and all housekeeping monitor outputs are routed by a 22-channel multiplexer (identified as INPUT MUX in Figure 7) to the gain selection circuits which properly scale those analog signals for input to the Analog to Digital Converter (ADC) described below). A 3-channel gain select multiplexer selects either the output of the 22-channel multiplexer or the output of one of two cascaded amplifiers, each with a gain of eight. The three multiplexed channels view the output of the 22-channel multiplexer at gains of 1, 8, and 64.

Analog to Digital Converter (ADC)

The ADC is a 12-bit, + 10 to − 10 V, successive approximation type converter, used over a + 5 to − 5 V 11-bit range only. The most significant bit (bit 11) indicates polarity of the signal, and the second most significant bit indicates a positive or negative overrange. Data reported to the Probe telemetry include the sign, two bits indicating the gain setting of the GSA, and nine bits of data from the ADC (bits 1 through 9 – bit zero is unused).

The microprocessor changes the gain of the GSA as required to obtain an on-scale reading for the ADC. The GSA is first set to its maximum gain of 64. If the processor detects that the ADC is in an overrange condition (input greater than + 5 or less than

– 5 V), it sets the GSA to a gain of 8. If this also leads to an overrange condition, the GSA is set to a gain of one.

Housekeeping Monitors

The housekeeping data that the NFR in the Probe telemetry stream is listed in Table III. The forward voltage drop change with temperature of a 1N4148 diode serves as the temperature sensor for the detector and electronics monitors (referenced in the table as DET and ET, respectively). The detector temperature sensing diode is mounted directly to the detector board on the rotating optics (see Figure 5). The hot black-body (HB) sensor is located on the back of a beryllium substrate on which the hot black-body heater resistor is painted. The ambient black-body low range (A1) and high range (A2) thermistors are located in the ambient black-body which is screw mounted and thermally coupled to the front housing wall. The window teperature (WT) sensor is located in the window housing structure on the rotating optics. The HB, A1, A2, and WT temperature sensors are Fenwal GB38SM43 thermistors.

Motor Driver

The motor driver is basically a pair of 28-V H-bridge circuits capable of driving up to 250 mA of reversible current through each of the two motor coils. The microprocessor controls the motor driver by writing a one into the appropriate latch bit to turn on one of two coils in one of two polarities. In addition to these four latch bits, there is one additional bit reserved for controlling eddy current damping by shorting one of the two coils. The exact time and duration of each motor coil pulse is controlled by the PROM software, and is turned, prior to burning PROMs, to obtain stable symmetric optical head rotation characteristics.

To obtain stable rotor motion characteristics under varying temperature conditions, the motor drive currents are stabilized by a current regulator circuit.

Optics Position Sensors

The rotor gear on the rotating optics has four slots cut into it so that four LED-photo transistor pairs mounted around the gear can determine if the rotor is at 0°, 90°, 180°, or 270° (± 5°). Only one photo-transistor will be turned on indicating the position of the rotor. If the correct transistor is not illuminated, this condition is reported in the data stream by setting the position error flag.

3.3. Analog Signal Characteristics

Radiation input to a given pyroelectric detector is absorbed by black paint covering the detector and subsequently heats the pyroelectric crystal, moving it towards a new thermal equilibrium temperature, which is ultimately attained when the crystal warms enough to conduct and radiate the absorbed power to its surroundings. The idealized DC pyroelectric detector generates charge across its capacitor plates which is proportional to the total temperature change since its last discharge. The charge which is generated slowly bleeds off through the load resistor and through the inherent leakage

of the pyroelectric crystal material. For the NFR detectors the load resistors are about a thousand times more important than the crystal losses, producing a charge decay (or droop) time constant of 0.36 s.

As a result of chopping the external radiation field by flipping the rotating optics, the NFR detectors are exposed to a radiation input approximately given by the waveform in Figure 8(a). During the transition between up and down views there is a brief period

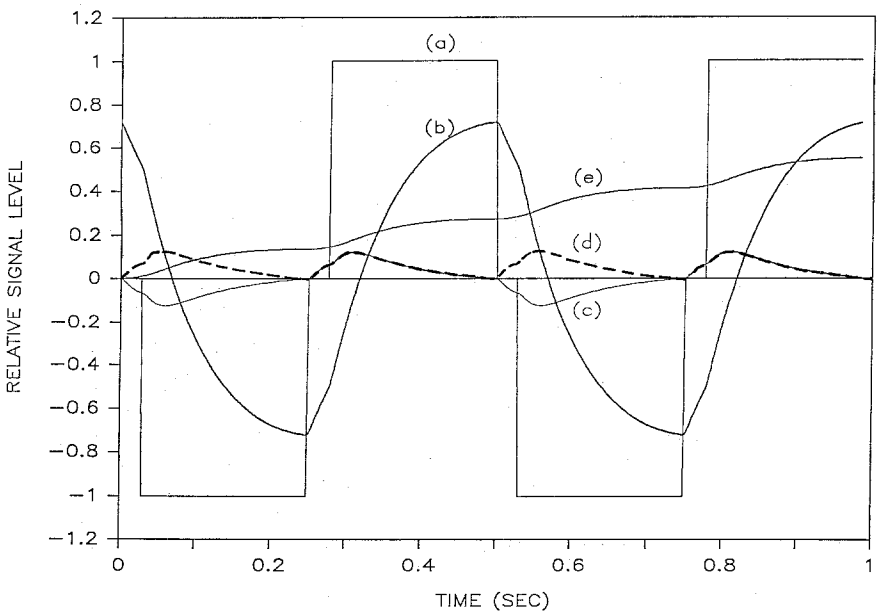

Fig. 8. Analog signal waveforms: (a) radiation input to detectors; (b) detector response; (c) after filtering by post amps; (d) after decommutation; (e) after integration. The plotted signals show the effects of filtering, decommutation, and integration, but not the rather large effects of amplification, which we excluded for clarity. These waveforms do not accurately simulate atmospheric input signals ((a) would have rounded corners during atmospheric measurements).

during which the detectors receive radiation from the wall of the front housing instead of the atmosphere; this contribution is clearly evident as the short flat spot in the irradiance profile. The approximate response of the detectors to the complete irradiance input waveform, shown in Figure 8(b), is a consequence of a thermal time constant of about 110 ms and an effective droop time constant of 1.1 s (the electrical droop time constant of 0.36 s appears to be partly offset from a long time constant component in the detector response). A rather drastic change in waveform is seen at the output of the post amplifier chain, shown in Figure 8(c), where the effects of the 16 Hz bandpass filter have resulted in a crude differentiation of the input signal. The decommutated and integrated waveforms are shown in Figures 8(d) and 8(e), respectively. What appear to be large distortions of the input signal should be thought of as signal conditioning to achieve maximum accuracy. The result of this signal processing is a very narrow bandpass filtering, with bandwidth of 0.09 Hz for 5.5 s of integration, which extracts

the amplitude of the 2-Hz fundamental which is proportional to the net radiation flux. As noted earlier, the filtering acts like a crude differentiator which, in combination with the integrator, has the beneficial characteristic of being insensitive to the details of the transition between upward and downward signal levels, and thus insensitive to asymmetries in mechanical motions.

Significant asymmetry errors can arise when the emission from the wall (or ambient blackbody) is considerably different from that of the atmosphere, and when the wall pulses seen during up and down transitions are not cancelled perfectly by the decommutation system because the pulses themselves are either of different width during up and down transits, or occur with different delay times relative to the decommutation waveform, or both. The resultant error is proportional to the difference between the average atmospheric flux, F_a, and the flux emitted by the wall, F_w. The error is then conveniently characterized in terms of the asymmetry factor, given by X_a = net flux error/$(F_w - F_a)$. By using large front housing apertures to minimize the size of the wall pulse, and by adjusting the motor pulse train program to symmetrize the delay of up and down wall pulses, the NFR asymmetry factor has been reduced to approximately 10^{-3} to 5×10^{-4}. When thermal models are used to estimate the expected difference between F_w and F_a during descent, the resultant asymmetry error is almost everywhere negligible compared to other sources of error.

4. Instrument Calibration

4.1. Equations for predicting instrument output

The object of the NFR calibration measurements is to define the instrument behavior sufficiently well so that, given a knowledge of the radiation field and the instrument environment, it is possible to predict the instrument output. The basic equations relating digital count output in a given channel to the external radiation field are essentially as follows:

$$C = Kf(T/T_0)\,(L_u - L_d)\,,$$

where K is an absolute calibration constant, $f(T/T_0)$ is a relative response function describing the instrument response dependence on detector temperature, and where $L_{u,\,d}$, the average radiances within the instrument FOV, are given by

$$L_{u,\,d} = \int_0^{\infty} s_\lambda \,\mathrm{d}\lambda \int_0^{\pi} \sin(\theta)\,\mathrm{d}\theta \int_0^{2\pi} \mathrm{d}\phi a_{u,\,d}(\theta, \phi) L(\theta, \phi, \lambda)\,,$$

where s_λ is the relative spectral response at wavelength λ; $a(\theta, \phi)$, relative angular response at θ (angle from vertical), ϕ (azimuth angle); $L(\theta, \phi, \lambda)$, spectral radiance at wavelength λ angles θ, ϕ, where s_λ and $a(\theta, \phi)$ are both normalized to have unit integrals. Because the NFR detector arrays are sealed in a rigid container, there is no dependence

of response on external atmospheric pressure, and crosstalk between spectral channels is small enough to allow relatively accurate corrections.

A conversion factor is needed to translate the net average radiance into an estimate for the net flux for a typical atmosphere; but this is an estimate based on model results and is not part of the instrument calibration. However, it has been a habit of the NFR investigators to assume a working conversion factor in calculating sensitivity. The practice can be illustrated for a flat radiation field, as in the extended area blackbody calibration (EABB) configuration. In this case $L(\theta, \phi, \lambda)$ is given by the Planck radiance function $B_\lambda(T)$ and the integral collapses to the form

$$L_{u,d} = \int_0^\infty s_\lambda B_\lambda(T_{u,d})\,\mathrm{d}\lambda \int_0^\pi \sin(\theta)\,\mathrm{d}\theta \int_0^{2\pi} \mathrm{d}\phi a_{u,d}(\theta, \phi) = \int_0^\infty s_\lambda B_\lambda(T_{u,d})\,\mathrm{d}\lambda\,,$$

which reduces to the spectrally weighted average of the net Planck radiance. For a spectrally flat broadband channel, the average net radiation (in the EABB configuration) is just

$$L_n = (L_u - L_d) = \frac{\sigma}{\pi}\,(T_u'' - T_d^4) = \frac{1}{\pi}\,(F_u - F_d) = \frac{1}{\pi}\,F_{\text{net}}\,.$$

But in a relatively opaque atmosphere the net radiance varies as the cosine of the nadir angle and can be written as

$$L(\theta) \approx \frac{1}{2\pi}\,(F_u + F_d) + \frac{3}{4\pi}\,(F_u - F_d)\cos(\theta)\,,$$

and thus,

$$L_n = L_n = L(45°) - L(135°) \approx \frac{3\sqrt{2}}{4\pi}\,(F_u - F_d) = \frac{3\sqrt{2}}{4\pi}\,F_{\text{net}}\,.$$

The measured responsivity of an NFR channel is usually quoted in terms of the ratio Counts/(F_{net}(EABB)). Since $3\sqrt{2}/4\pi$ is only 6% larger than π^{-1}, the measurement sensitivity to the EABB flux difference is almost correct as a measure of sensitivity to atmospheric net flux. Appropriate conversion factors will be applied in deriving the best estimate of the descent profile of atmospheric flux.

4.2. Basic calibration measurements

To calculate the instrument output according to the above equations requires the following basic measurements:

(1) Relative angular response for each detector channel.
(2) Relative spectral response for each spectral band.
(3) Relative crosstalk coefficients between neighboring channels.
(4) Relative response versus temperature for each channel.

(5) Absolute responsivity measurements for each channel using a source which fills the NFR field of view.

Methods and sample results are described in the following paragraphs.

Relative Angular Response Measurements

Angular response was measured using a chopped stationary source of 4° angular diameter in conjunction with an articulating mount for the NFR optical head. The articulation was accomplished with crossed rotators scanned by computer control to map the solid angle domain with 2° resolution. The optical head was mounted so that the center of the diamond window remained fixed during the articulation. The rotating optics assembly was held motionless by disabling NFR motor power; a modulated signal was instead obtained by chopping the radiation source at a 2-Hz rate in synchronization with the NFR decommutation signal. This allowed the NFR data system to acquire the angular response data, while minimizing the wear and tear on the NFR gears. The angular scan was made twice, once using a short wavelength source consisting of an integrating sphere illuminated by a quartz-halogen lamp, and once using a long wavelength source which is just a small black-body operating at 128 °C. A sample response function is shown in Figure 9. A consequence of the NFR optical design (shown in Figure 3) is that the maximum response of each detector is in a slightly different location (adjacent detectors are separated by 5–6°).

Relative Spectral Response

Typical spectral response results are shown in Figures 10 and 11 (results from the final flight instrument calibration were not available at the time of this writing). The relative spectral response measurements were generally made using appropriate short or long wave sources, a monochromator to select wavelengths, and a reference detector to measure the monochromator output for comparison with the NFR measurements. Our primary reference detector is a deuterated triglycene sulfate (DTGS) pyroelectric detector with a thorium fluoride-coated KBr window. This detector was calibrated by D. Stierwalt at the Naval Oceans Systems Center (NOSC) in San Diego. Stierwalt's calibration is based on comparisons with a standard spectrally flat detector which uses a blackened conical receiver (Eisenman *et al.*, 1963; Eisenman and Bates, 1964). A conical detector was borrowed from the NOSC laboratory for additional comparisons at Wisconsin. Our comparisons and those at the NOSC laboratory were in significant disagreement concerning the long wavelength fall off in detector response. For example, at 30 μm our version of the detector response was 40% greater than the NOSC value. This discrepancy was investigated by making broadband filter measurements at Wisconsin, and performing a second calibration using a 2-Hz chopping frequency at NOSC (normally a 10-Hz chopping frequency is used at NOSC). Although more recent results are in much better agreement (the discrepancy is now less than 10% at 30 μm), this remains an area of study.

Our spectral response measurements used a quartz halogen source between 0.25 μm and 3 μm, and a 1000 K silicon carbide globar for wavelengths from 3 μm to about

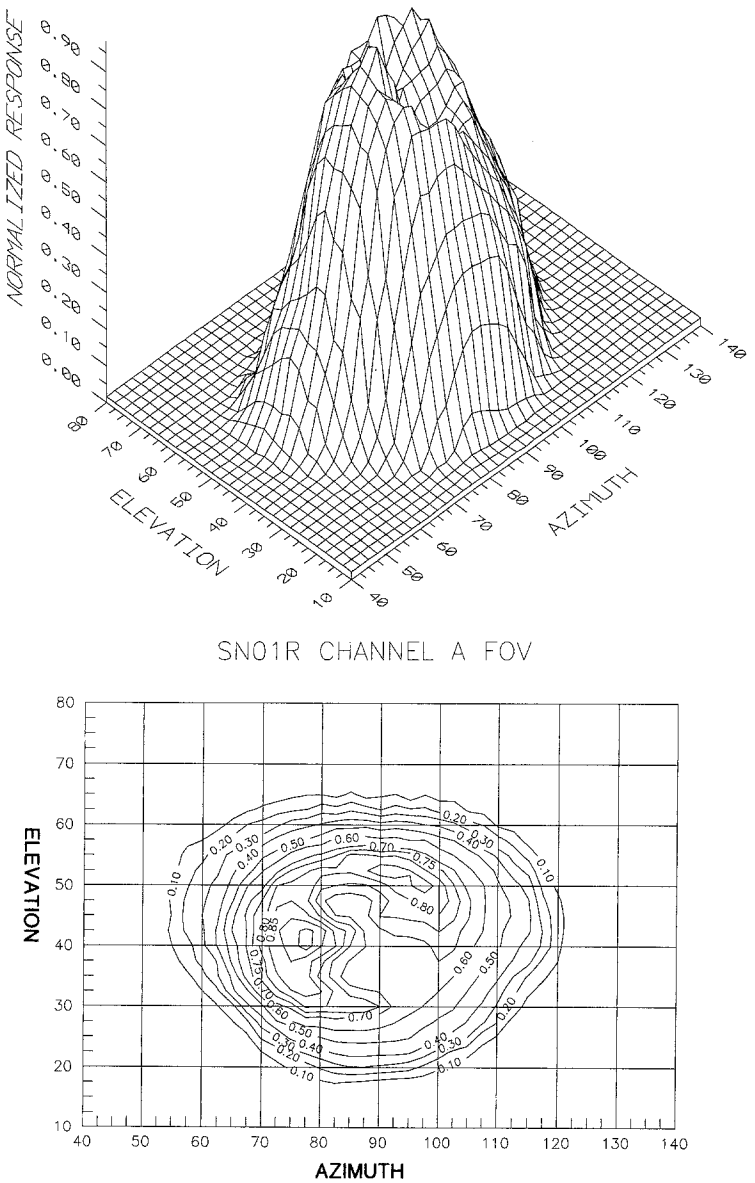

Fig. 9. Sample angular response functions. Here elevation refers to the angle above the horizon and azimuth refers to angle about the vertical (90° azimuth corresponds to the position of the NFR optical head rotation axis). During the early part of descent the Sun will have an elevation angle of 25°, and may intrude into the edge of the NFR field of view.

38 μm. Because of large variations in source output as a function of wavelength, it was necessary to use stray light filters at the shortest wavelengths, and neutral density filters at intermediate wavelengths, the latter to maintain on-scale detector signals. Multiple gratings and order-sorting filters were also required. Slit widths were chosen to obtain

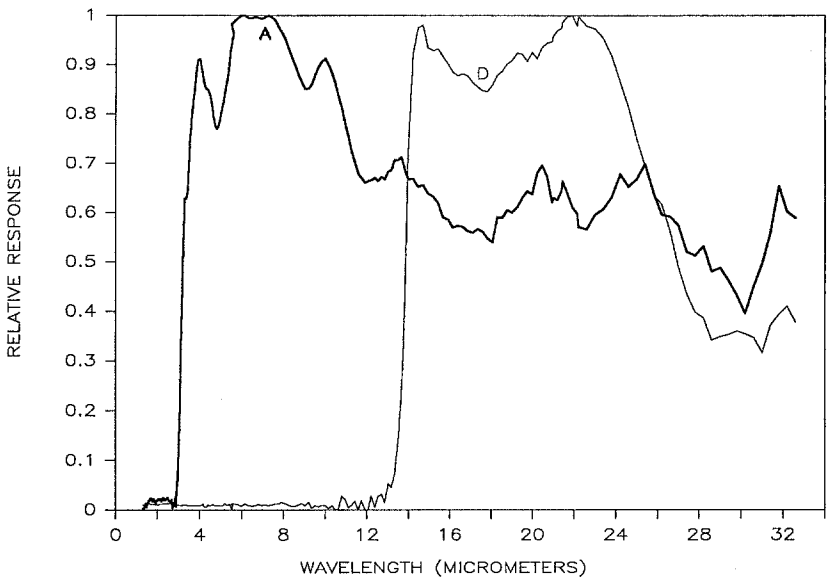

Fig. 10. Relative spectral response functions for NFR long wavelength channels *A* and *D*, normalized to have a maximum value of one. These were measured for the SN01R instrument prior to installation of new detectors. Analysis of final flight calibration results will yield very similar curves.

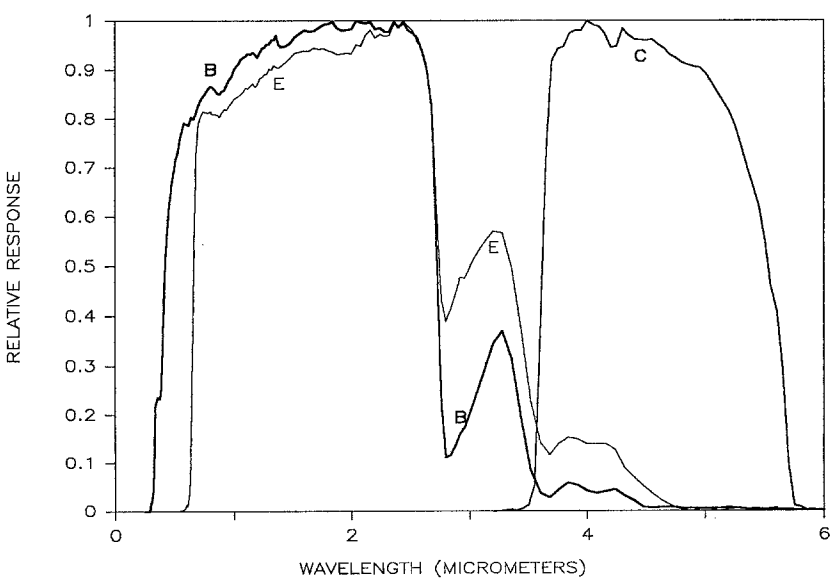

Fig. 11. Relative spectral response functions for NFR channels *B*, *E*, and *C*. Channels *B* and *E* use colored glass filters, while C uses an interference filter and a long wave CaF_2 blocker. Normalization and instrument used are the same as for Figure 10. Analysis of final flight calibration data and additional measurements using the spare NFR instrument and spare filters will allow us to define the spectral response much better at longer wavelengths.

high monochromator throughput with moderate spectral resolution (typically 4–5% of wavelength). Wavelength calibration was checked with a mercury vapor lamp.

Although all the radiation exiting the monochromator was focussed on the active area of the reference detector, the NFR detectors, because of optical limitations, could only sample a portion of the radiation. Because the radiation entering the NFR is not perfectly scrambled, sampling does lead to small spectral errors, the magnitude of which can be estimated by repeating scans with different NFR orientations, and by comparing overlapping scans with successive gratings.

Accurate measurements of system-level spectral response beyond approximately 35 μm were not practical with the monochromator system because of signal-to-noise limitations. To limit uncertainties in relative spectral response at longer wavelengths we also used broad-band and diamond dust cut-on filters (with known transmissions) in combination with a known black-body source. To refine the long wavelength spectral response characteristics these measurements of the flight instrument response will be supplemented by additional measurements of the spare instrument and spare filters and detectors.

Relative Crosstalk Coefficients

Crosstalk coupling coefficients were determined by exposing the NFR to spectrally independent sets of stimuli, then measuring the response of all channels. For any given stimulus vector there exists a direct detector response vector **R**, which is transformed by crosstalk matrix A_{ij} to a gain-corrected count response vector **C′**, with elements

$$C_i' = \frac{C_i}{g_i} = \sum A_{ij} R_j ,$$

where g_i is a gain conversion fator for channel i. When it is possible to stimulate directly just a single channel, then the coupling coefficients are trivially determined by the relationship

$$A_{ij} = \frac{C_i/g_i}{R_j} \approx \frac{C_i/g_i}{C_j/g_j} .$$

The approximation of R_j by C_j/g_j is warranted because the crosstalk coefficients are rather small (just a few tenths of 1% or less).

Relative Temperature Dependence

To measure responsivity as a function of temperature the NFR optical head was mounted on a thermoelectric cooler within a sealed chamber which was evacuated to maximize the performance of the temperature control system. While exposed to a constant radiation source the instrument temperature was changed from − 20 °C to + 50 °C. The test was carried out in two parts: first, extended area black-body sources were used and the NFR motor was used to chop between the two soures; and second, an external chopped quartz-halogen source was used and the NFR motor was turned

off. A comparison of these two test results shows that the NFR motor operation does not vary with temperature sufficiently to have a significant effect on responsivity. We did find, however, that the NFR spectral response does vary somewhat with temperature, leading to different temperature dependencies in different channels. Figure 12

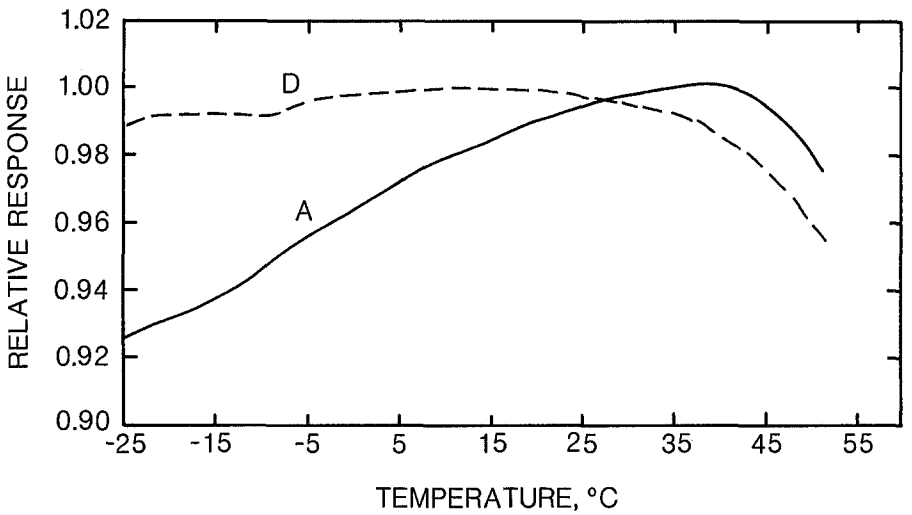

Fig. 12. Temperature dependence of responsivity for NFR channels *A* (3–500 μm) and *D* (14–35 μm). Results were obtained using Extended Area Black-Body (EABB) sources and NFR rotational chopping. The difference between these two curves is presumably a result of temperature dependence in the spectral characteristics of channel *D*. The response curve of channel *A* is dominated by the relative temperature dependence of detector responsivity. Both curves were normalized to have a maximum of one.

compares the response of channel *A* with that of channel *D*. Most channels, when illuminated mainly with in-band radiation, behave approximately like channel *A*. The responsivity decline at temperatures beyond 50 °C is sufficiently uncertain to warrant further investigation using the spare detector package.

Absolute Responsivity Measurements

The absolute calibrations used sources of well-known spectral content which uniformly fill the field of view of the NFR, and which are spectrally shaped to provide strong in-band stimulation.

Long Wave Channels. Long wavelength channels *A* (3.5–500 μm) and *D* (14–35 μm) were calibrated using two distinct black-body source configurations: one configuration uses a pair of extended area black-body (EABB) sources made by Advanced Kinetics, Inc. (Costa Mesa, CA), the second configuration used a pair of black-body cavities adapted from soruces used on a previous University of Wisconsin Pioneer Venus experiment (Sromovsky *et al.*, 1980). In both cases the pair of sources was arranged to fill the NFR field of view at 'up' and 'down' positions, and the NFR flipped between

them using the rotating optical system. The EABB sources are 6-inch × 6-inch aluminum plates with a blackened honeycomb emitting surface and three independent thermoelectric servo systems trying to maintain a constant and spatially uniform temperature. Temperature measurements were made using platinum resistance thermometers. The emittance of the EABB sources is better than 0.995 by manufacturer calculation, but not independently measured. A concern with the EABB sources is the existence of temperature gradients within the aluminum radiating plate. The three independent temperature monitor readouts on each plate typically differ by 0.1–0.2 K. The platinum resistance sensors within the EABBs may also have experienced some minor shift in calibration due to repetitive thermal cycling. A comparison with recently calibrated precision thermistors indicates that such a shift is probably no more than 0.1 to 0.2 K. Both emissivity and temperature uncertainties are not expected to create calibration errors greater than 1%, although this estimate itself is sufficiently uncertain to warrant comparison with the independent set of cavity calibration sources.

The cavity sources are relatively small and thick-walled, leading to very uniform temperatures within the cavity. The cavity temperatures are monitored with YSI 44031 precision thermistors with a guaranteed interchangability of 0.1 K with respect to an absolute temperature scale. To minimize offset errors we compared a set of six thermistors, and selected four which were in closest agreement for use as cavity monitors (these differed by a maximum of 0.03–0.06 K). The cavity emittance, calculated according to formulas developed by Sydnor (1970), using paint properties measured by Stierwalt (1966), is estimated to be approximately 0.99, not counting the additional enhancement resulting from reflection of cavity radiation off the NFR back into the cavity. The disadvantage of the cavity sources relative to the EABB sources is that the former can only be heated above room temperature, while the latter can be cooled as well as heated.

The results of these calibrations for the SN02R2 instrument, summarized in Table IV, are very encouraging in that both source configurations lead to essentially the same calibration for both longwave channels (within 0.2% and 0.5% for *A* and *D*, respectively). This is better agreeement than the estimated uncertainty of about 1% (based on a temperature difference uncertainty of 0.2 K and an emissivity uncertainty of 0.5%). The responsivities in this table are calculated by dividing the digital count output by the net flux input, where the net flux input is 'in-band' net flux calculated by integrating the source emission spectrum over the relative spectral response of each channel, using a normalization of unity at the maximum responsivity. This able does not show EABB and cavity calibration results for channels *B* and *E* because the long wave sources are poorly suited for calibration of these short wave channels. (Most of the source energy is outside their spectral bandpasses making in-band flux calculations extremely dependent on details of the long wave cutoffs of these channels.)

Short Wave Channels. The calibration of the solar channels *B* (0.3–3.5 μm) and *E* (0.6–3.5 μm) is based on a spectral irradiance standard which illuminates a standard diffusing plate filling the NFR field of view. The irradiance standard is a 40 W quartz-

TABLE IV

Absolute calibration results. Columns labelled EABB and Cavity contain results obtained with long wavelength sources. The column labelled QH contains calibration results using a quartz-halogen standard lamp. The column labelled Globar lists calibration data obtained with a 1000 K globar source illuminating a gold integrating sphere and using a reference detector to measure the sphere output. Note the excellent agreement between EABB and cavity calibration results, and between these results for channel C and that obtained with a filtered globar source.

Channel	Responsivity in counts $W^{-1}\,m^{-2}$			
	EABB	Cavity	QH	Globar
A	241.7	242.2		
B			766.5	
C	1468.4	1475.0		1443.5
D	807.4	811.2		
E			1410.0	

halogen lamp calibrated by Optronics Laboratories, Inc. of Orlando Florida. The calibration extends from 0.25 to 3.5 μm, but is most accurate at wavelengths less than 2.5 μm. A water filter was placed between the lamp and the diffuser plate to block radiation at uncalibrated and at inaccurately calibrated wavelengths. The spectral transmission of the water filter was measured using the monochromator and a pyroelectric detector. The diffuser is a freshly prepared 6 × 10-inch × 5 cm thick Halon surface compressed to a density of 1 g cm^{-3} to obtain standard reflectivity properties (Weidner *et al.*, 1985). Over most of the visible spectrum, the surface reflectivity is approximately 0.99. Given the known source intensity, transmission of the water filter, distance to the diffusing screen, and reflection properties of the screen, it is possible to calculate the in-band flux in the short wave channels with an RSS uncertainty of about 2.5% (calculated as the RSS of the following contributions: 1.3% NBS uncertainty, 1% transfer uncertainty, 1.75% uncertainty in water filter transmission, 0.5% uncertainty in surface reflectivity). The calibration was performed twice: once with the radiation source chopped and the NFR rotor immobilized, and a second time with the source steady and the NFR chopping. The results of the absolute calibration of channels *B* and *E* are shown in Table IV.

Channel C Calibration. The excess thermal channel (*C*), with a spectral bandpass from 3.5 to 5.8 μm, was calibrated using both long wavelength broadband sources and also using a restricted wavelength source. The restricted source used a 1000 K globar filtered to restrict radiation to be within the channel *C* spectral band, then input to a gold diffusing sphere to provide the angular distribution needed to fill the NFR field of view. Because the output of the integrating sphere cannot be calculated with sufficient accuracy, it had to be measured. This was done using a reference detector calibrated at short wavelengths (using the same procedure as carried out to calibrate channels *B*

and E) and adjusted for its relative spectral response. The uncertainty of this calibration is approximately 3.4%, estimated as the root sum square of the following uncertainties: 2.5% uncertainty in reference detector calibration at calibration wavelengths, 2% uncertainty in relative spectral response of the reference detector, and 1% variation in integrating sphere output due to NFR-reference detector reflectivity differences). The result of this calibration differs by only 1.9% from the average calibration using cavity and EABB broadband sources (see Table IV). This is a gratifying agreement between two completely independent calibration methods, one ultimately related to an NBS spectral irradiance standard, and the other dependent on temperature measurement and emissivity calculations.

5. Performance Expectations

5.1. Signal characteristics

The Galileo Probe will enter the atmosphere near the evening terminator; the initial solar zenith angle for NFR measurements will be approximately 65° and will increase with time as Jupiter's rotation carried the Probe into sunset, which will occur near the 10-bar level. Depending on the Probe spin rate, the strong azimuthal variations in scattered solar radiation may be evident in channels B and E above the 1-bar level (Tomasko and Doose, 1988). Deeper in the atmosphere, the direct solar beam and azimuthal variations will both become insignificant. Gains on channels B and E are low enough to handle relatively large azimuthal variations, but not low enough to handle the direct solar beam (which will in the worst case only be near the edge of the NFR field of view (see Figure 9).

Predicted net flux profiles under expected descent conditions are shown in Figure 13. (These are only tentative estimates which will be considerably refined prior to Jupiter encounter.) Profiles for long wave channels A, D, and C (Pollack, 1986) are from calculations which do not include cloud opacity. Profiles for short wave channels B and E (Tomasko and Doose, 1988) do include effects of cloud opacity and haze, with boundaries as indicated in the figure. Expected measurement noise in individual net flux data samples is indicated by error bars on each profile. Errors due to calibration uncertainties are not shown. Detector noise (actually, this is mainly Johnson noise in the load resistors) is almost everywhere the dominant noise source, and quantization and asymmetry errors are almost everywhere insignificant. During thermal transients, there may also be noise contributions from detector arcing, as described later.

At the top of Figure 13 is a tabulation of the number of samples expected for each atmospheric layer. For example, within the NH_3 ice cloud between 300 and 700 mb we expect 29 net flux measurements, but less than two each of Up Flux, Black-body Calibrate, and Analog Zero measurements. The vertical resolution of net flux measurements is high enough to allow some noise reduction through averaging, especially at the higher pressures (where it is needed the most). Uncertainty in calibration, offset correction, and crosstalk couplings are, of course, systematic errors which cannot be reduced by vertical averaging.

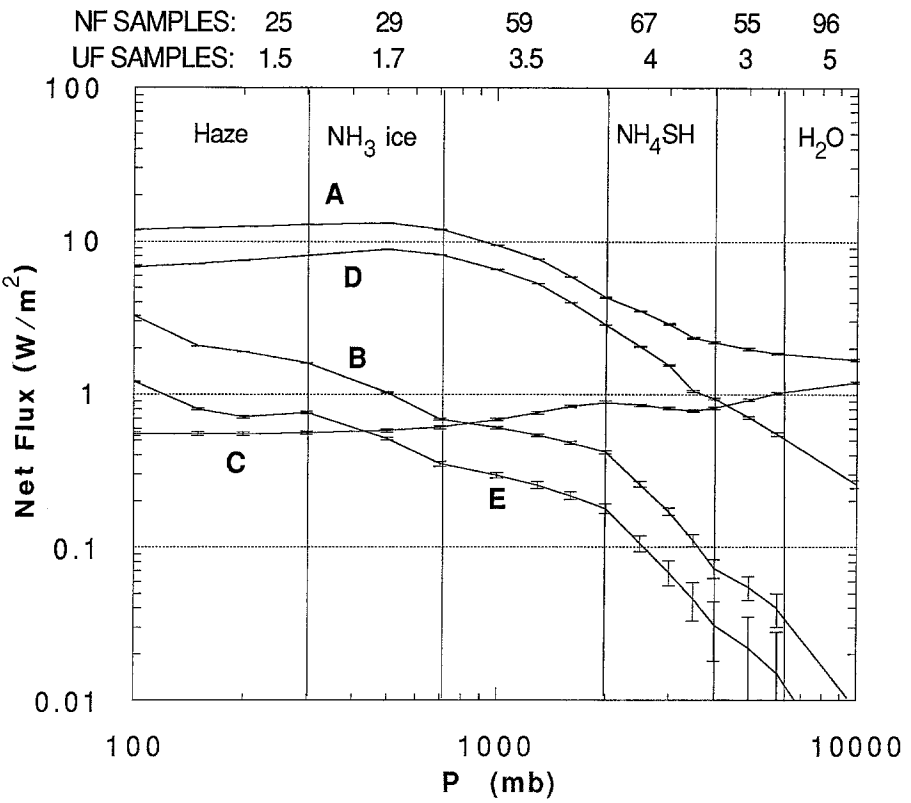

Fig. 13. Predicted profiles of net flux versus pressure during descent into Jupiter's atmosphere. Calculations for channels *A*, *D*, and *C* did not account for cloud opacity. Clouds were included in simulating measurements in the solar channels *B* and *E*. The cloud and haze boundaries used in these calculations are indicated by vertical lines and labelled by cloud composition. The number of samples of net flux (NF) and up flux (UF) data in each layer is listed across the top of the figure. Error bars indicate the expected measurement noise. Calibration errors are not included. The rapid decline of signal in channels *B* and *E* near 10 bars is a consequence of the Sun's setting.

5.2. Detector arcing

NFR detector crystals develop potential differences proportional to the rate of change of detector temperature and to the bleed resistance. The electroded part of the crystal does not develop a substantial potential because the load resistors are very efficient at bleeding off the charge. The time constant for bleeding off charge from the unelectroded regions of the crystals is about 1000 times longer, so that thermal ramp-induced potentials can become large enough to cause sudden discharges. These discharges can become large enough so that a single event can invalidate a 5.5-s data sample. Fortunately, these events are likely to be relatively infrequent, occurring mainly during the second 5 min of descent, between the point of the maximum negative thermal ramp and the point of minimum detector temperature. This covers an approximate pressure range from 0.5 to 1.5 bars (see Figure 13). Only channels *C* and *E* exhibited arcing noise during laboratory testing of the flight instrument.

5.3. Expected performance of the detector package seal

The first objective of the seal, preventing pressure perturbations from reaching the detectors, appears to be met even with a relatively poor seal. This inference is based on comparing wind tunnel tests of an unsealed detector with those of a poorly sealed detector leaking at a rate of approximately 10^{-5} cc s^{-1} (xenon equivalent). A much better seal is required to prevent large crosstalk couplings and responsivity variation. With any more than 100 mb of He in the detector package crosstalk would be five times the vacuum level and responsivity would be degraded by 15%. (Hydrogen has approximately the same effect as He.) To make these effects negligible the seal should keep the thermal conductivity of the gas within the detector package no higher than that of air (about $\frac{1}{5}$ that of helium).

The upper bound of the detector leak rate measured by mass spectrometry shortly after sealing (in February 1989), is approximately 7×10^{-10} cc (of Xe at STP) s^{-1} with a pressure difference of approximately 840 mb. Given an initial volume of approximately 0.033 cc of gas (the internal volume of the detector package), and assuming that the leak is viscous in nature, we find that after 6 years of leaking the detector package will still retain about 100 mb of Xe. We measured the rate at which helium leaks into the package by watching the NFR response to a fixed radiation source as the helium diffuses into the detector package. After 23 hours of exposure to 1 bar of helium we saw a response drop of only 0.5%, implying a maximum He diffusion leak rate of about 10^{-7} cc s^{-1} (this rate takes several hours to become established). Because tests with a mockup detector seal show no significant difference between He and H_2 diffusion rates, we can conclude that no more than 10–20 mb of Jovian He and H_2 combined will leak into the detector during descent. This is well below the level which could affect detector response, especially in the presence of 100 mb of Xe, which buffers the conductivity of the lighter gases.

Acknowledgements

This difficult experiment would not have been possible without considerable effort and dedication by many individuals. Foremost among them is Robert W. Boese, the original P.I. from Ames Research Center, who conceived and nurtured this experiment until his untimely death in December 1985. Others from Ames Research Center deserving thanks are Jim Pollack for encouragement and technical support at several critical times, and Rick Twarowski and Benny Chin, who guided us through many complex difficulties in managing and funding instrument development.

At Martin Marietta we thank DeWane Shumaker (optical head fabrication), Tony Knight (management), Ruth Amundsen (engineering support and management), Tom Hopkins (quality assurance), Steve Shertz (engineering support), and Briggs Cunningham (program assistance).

At the University of Arizona we thank Martin Tomasko, Peter Smith, and Lyn Doose for excellent science impact evaluations and calibration support.

At the University of Wisconsin-Madison we wish to thank Patrick Fry (software,

calibration, testing, data analysis), Donald Thielman (electronics design and testing), Jeffrey Vian (mechanical design, detector development support, and testing), Scott Ellington (electronics design), Jerry Sitzman (electronics design and testing), and Mike Dean (parts procurement).

We also thank the Galileo Project for providing support and guidance necessary to reach a satisfactory conclusion to this difficult effort. Bill O'Neil's efforts were particularly helpful.

The work carried out by the University of Wisconsin was supported by NASA Contract NAS2–12078.

References

Eisenman, W. L. and Bates, R. L.: 1964, 'Improved Black Radiation Detector', *J. Opt. Soc. Am.* **54**, 1.

Eisenman, W. L., Bates, R. L., and Merriam, J. D.: 1963, 'Black Radiation Detector', *J. Opt. Soc. Am.* **53**, 729.

Hunten, D. M., Colin, L., and Hansen, J. E.: 1986, 'Atmospheric Science on the Galileo Mission', *Space Sci. Rev.* **44**, 191.

Pollack, J.: 1986, personal communication.

Seiff, A. and Knight, T. C. D.: 1992, 'The Galileo Probe Atmosphere Structure Instrument', *Space Sci. Rev.* **60**, 203 (this issue).

Sromovsky, L. A., Revercomb, H. E., and Suomi, V. E.: 1980, 'Pioneer Venus Small Probes Net Flux Radiometer Experiment', *IEEE Trans. Geosci. Rem. Sens.* **GE-18**, 117.

Stierwalt, D. L.: 1966, 'Infrared Spectral Emittance of Optical Materials', *Appl. Optics* **5**, 1911.

Sydnor, C. L.: 1970, *A Numerical Study of Cavity Radiometer Emissivities*, NASA Technical Report 32–1463.

Tomasko, M. and Doose, L.: 1988, personal communication.

Weidner, V. R., Hsia, J. J., and Adams, B.: 1985, 'Laboratory Intercomparison Study of Pressed Polytetrafluoroethylene Powder Reflectance Standards', *Appl. Optics* **24**, 2225.